WELDING RESEARCH

SUPPLEMENT TO THE *WELDING JOURNAL*, OCTOBER 1987

Sponsored by the American Welding Society and the Welding Research Council

Effect of Rapid Solidification on Stainless Steel Weld Metal Microstructures and Its Implications on the Schaeffler Diagram

Rapid cooling has a profound effect on weld metal microstructures, making predictions from conventional constitution diagrams impossible

BY S. A. DAVID, J. M. VITEK AND T. L. HEBBLE

ABSTRACT. An investigation was carried out to determine the effect of rapid solidification on the weld metal microstructure of austenitic stainless steels and its implication on the ferrite constitution diagram. A wide variety of stainless steels were laser beam welded at different welding speeds and laser power levels. The results indicate that both weld pool cooling rate and the postsolidification solid-state cooling rates have a profound effect on the microstructures. For the steels investigated, the microstructures ranged from duplex austenite (γ) + ferrite (δ) to fully austenitic or fully ferritic. These microstructures were found to be sensitive to both cooling rates and composition. The observed results are rationalized based on rapid solidification theory.

Observations of this investigation indicate that solidification rates and postsolidification cooling rates have a profound effect on the observed microstructures, thus making it impossible to predict the microstructures of rapidly cooled weld metal from the conventional constitution diagrams. The influence of the observations made in this investigation on the Schaeffler diagram is demonstrated, and possible corrections to the constitution diagram incorporating the cooling rate effects are proposed.

S. A. DAVID and J. M. VITEK are with the Metals and Ceramics Division, Oak Ridge National Laboratory, Oak Ridge, Tenn. T. L. HEBBLE is a member of the Computer Sciences Division, Martin Marietta Energy Systems, Inc.

KEY WORDS

Rapid Solidification
Ferrite Constitution
Constitution Diagram
Weld Pool Cooling
Postsolidification
Solidification Rates
Microstructure Effect
Rapid Cooling
Ferritic-Austenitic
Schaeffler Diagram

Introduction

Austenitic stainless steel is an extensively used engineering material for corrosion resistance and good low- and elevated-temperature mechanical properties. A significant problem in the production of fully austenitic stainless steel welds is their tendency toward hot cracking. To minimize this tendency, the compositions of weld filler metals are generally modified to produce small amounts of delta (δ) ferrite in the as-welded microstructure. Such compositional changes promote the formation of ferrite as the primary solidification phase. Schaeffler (Ref. 1) and DeLong (Ref. 2) constitutional diagrams are successfully used to predict the ferrite content in austenitic stainless steel welds at room temperature. Also, a constitutional diagram has been developed for castings (Refs. 3–5). These diagrams are all used to roughly estimate the ferrite level, based on composition. The diagrams are based on the use of chromium equivalents (Cr_{eq}) and nickel equivalents (Ni_{eq}) which, with proper weighting factors, group together the ferrite-form-

Table 1—Compositions of the Welds (wt-%)

Steel AISI-Type	Cr	Ni	Mn	C	Si	P	S	Mo	Ti	Ta	Nb	Cr_{eq}	Ni_{eq}	$\frac{Cr_{eq}}{Ni_{eq}}$
304-A	18.85	9.54	1.38	0.05	0.51	0.023	0.019					19.62	11.73	1.67
304-B	18.16	8.63	1.28	0.06	0.72	0.032	0.007					19.24	11.07	1.74
308-A	20.12	9.72	1.78	0.04	0.38	0.023	0.005	0.06				20.75	11.81	1.76
308-B	19.17	10.57	1.92	0.06	0.72	0.045	0.016		0.56			20.25	13.33	1.52
309-A	23.84	12.75	1.80	0.05	0.39	0.024	0.008					24.43	15.15	1.61
309-B	23.01	13.41	2.08	0.02	0.46	0.011	0.003	0.01	0.11	0.01	0.01	23.72	15.05	1.58
316-A	17.01	11.50	1.86	0.04	0.30	0.016	0.012	2.30				19.76	13.63	1.45
316-B	19.25	12.73	2.22	0.03	0.45	0.042	0.018	2.34	0.39			22.27	14.74	1.51
312-A	28.92	8.44	1.24	0.13	0.43	0.018	0.004	0.15				29.72	12.96	2.29
312-B	29.72	8.78	1.68	0.11	0.39	0.025	0.005	0.20				30.51	12.92	2.36
347-A	19.5	10.0	1.50	0.06	0.60	0.018	0.020	0.10			0.70	20.85	12.55	1.66
347-B	19.38	8.66	1.21	0.04	0.35	0.010	0.019	0.05		0.01		19.96	10.47	1.91
446-A	26.62	0.34	1.15	0.14	0.45	0.022	0.016	0.10				27.40	5.12	5.36
310-A	26.73	21.15	1.64	0.11	0.50	0.014	0.009	0.05				27.53	25.27	1.09
310-B	25.62	19.18	0.90	0.03	0.42	0.013	0.005	0.15				26.40	20.53	1.29

ing elements such as chromium, silicon and molybdenum and the austenite-forming elements such as nickel, carbon and manganese, respectively. However, these diagrams do not take into account the effect of weld metal solidification rate.

Rapid solidification of materials may produce microstructures during solidification that are markedly different from those observed during conventional solidification. During rapid solidification, the mode of solidification may change, the microstructural features are much finer, and solute segregation patterns may be greatly altered. During welding, which is one form of solidification processing, the cooling rates may vary from 10^2 to 10^6 °C/s, depending on the welding process. For conventional welding processes such as gas tungsten arc (GTA) and submerged arc (SA), cooling rates may be on the order of 10^3 °C/s. However, in the high-power beam processes such as electron beam (EB) and laser beam welding, it is common to encounter cooling rates on the order of 10^4 to 10^6 °C/s.

It has been shown before that high cooling rates have altered the microstructures in stainless steel welds (Refs. 6–8). Work on Type 303 stainless steel has shown that extensive microstructural modification may occur during the rapid solidification of fine powders (Ref. 9). Also, large degrees of undercooling have been shown to alter dramatically the structure of Type 316 stainless steel (Ref. 10). The purpose of this investigation is to characterize and understand the extent of modifications in microstructures that occur during rapid solidification of a wide variety of austenitic stainless steel welds. The work is also aimed at modifying the Schaeffler diagram to incorporate the microstructural changes observed as a function of weld metal cooling rates.

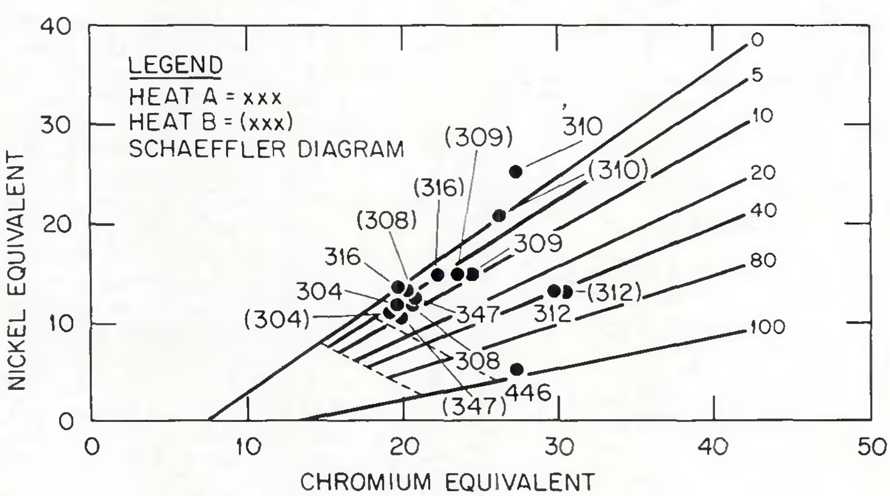

Fig. 1—Schaeffler diagram showing the location of the various steels selected for investigation on the diagram

Experimental Procedure

Materials

The materials used in this investigation were commercial austenitic stainless steel filler metal alloys. The compositions of the alloys are given in Table 1. These alloys were selected to provide for different solidification modes. Two heats of all but one (Alloy 446) of the alloys were evaluated to provide a range of compositions within the specifications for a given steel. The different heats will be distinguished by referring to each alloy with an A or B suffix. The ferrite-forming tendencies of these alloys are reflected in their net chromium and nickel equivalents, calculated as (Ref. 1)

$$Cr_{eq} = Cr + Mo + 1.5\ Si + 0.5\ Nb$$
$$Ni_{eq} = Ni + 30\ C + 0.5\ Mn$$

where the symbols represent the elemental compositions in weight percent. The ratio of Cr_{eq}/Ni_{eq} for each alloy is also given in Table 1. The location of each alloy composition on the Schaeffler constitution diagram is shown in Fig. 1. As the Cr_{eq}/Ni_{eq} ratio increases, the ferrite-forming tendency of the alloy also increases.

Welding

Selected filler metal alloys were arc melted, drop cast into rectangular ingots and cold rolled down, with intermediate annealing at 1050°C (1922°F), to 0.51-mm (0.02-in.) thick sheets. Autogenous laser beam welds were made on 5- × 5-cm (2- × 2-in.) coupons using a pulsed Nd:YAG laser (Raytheon Model SS-500) capable of delivering an average power of 400 W. A 6-in. (152-mm) lens was used to focus the beam sharply onto the specimen surface. A pulse length of 1 ms and pulse rate of 200 pps were used in an argon atmosphere. In order to vary the heat input, and hence the cooling rate, two laser power levels of 190–200 and 110–120 W were used. Welding speeds ranging from 12.7 to 254 cm/min (5 to 100 ipm) were used.

Microstructural Characterization

Microstructural characterization was done by optical, as well as transmission electron, microscopy. Metallographic specimens were etched using a solution containing HNO_3 and H_2O. The micro-

Table 2—Summary of Microstructures

Laser Power, W	Welding Speed, cm/min	Estimated Cooling Rate $\times 10^6$ °C/s	Series A								Series B						
			304 [1.67][a]	308 [1.76]	309 [1.61]	316 [1.45]	347 [1.66]	312 [2.29]	446 [5.36]	310 [1.09]	304 [1.74]	308 [1.52]	309 [1.58]	316 [1.51]	347 [1.91]	312 [2.36]	310 [1.29]
190–200	12.7	0.07	$\gamma+\delta$ (9.0)[b]	$\gamma+\delta$ (13.5)	$\gamma+\delta$ (11.0)	$\gamma+\delta$ (15.0)	$\gamma+\delta$ (13.0)	$\gamma+\delta$ (80.0)	$\gamma+\delta$ (90.0)	γ	$\gamma+\delta$ (10.0)	$\gamma+\delta$ (12.0)	$\gamma+\delta$ (12.0)	$\gamma+\delta$ (19.0)	$\gamma+\delta$ (10.0)	$\gamma+\delta$ (90.0)	γ
	50.8	0.28	$\gamma+\delta$ (5.0)	$\gamma+\delta$ (13.0)	$\gamma+\delta$ (14.0)	γ	$\gamma+\delta$ (4.0)	$\gamma+\delta$ (90.0)	$\gamma+\delta$ (97.0)	γ	$\gamma+\delta$ (3.0)	$\gamma+\delta$ (2.0)	$\gamma+\delta$ (23.0)	$\gamma+\delta$ (23.0)	$\gamma+\delta$ (6.0)	$\gamma+\delta$ (88.0)	γ
	127.0	0.71	$\gamma+\delta$ (2.0)	$\gamma+\delta$ (1.5)	$\gamma+\delta$ (10.0)	γ	γ	δ	δ	γ	γ	γ	$\gamma+\delta$ (24.0)	$\gamma+\delta$ (21.0)	γ	$\gamma+\delta$ (90.0)	γ
	190.5	1.1	γ	γ	$\gamma+\delta$ (6.0)	γ	γ	δ	δ	γ	γ	γ	$\gamma+\delta$ (16.0)	$\gamma+\delta$ (16.0)	γ	δ	γ
	254.0	1.4	γ	γ	$\gamma+\delta$ (5.0)	γ	γ	δ	δ	γ	γ	γ	$\gamma+\delta$ (9.0)	$\gamma+\delta$ (6.0)	γ	δ	γ
110-120	12.7	0.12	$\gamma+\delta$ (10.5)	$\gamma+\delta$ (13.0)	$\gamma+\delta$ (15.0)	$\gamma+\delta$ (13.0)	$\gamma+\delta$ (14.0)	$\gamma+\delta$ (84.0)	$\gamma+\delta$ (90.0)	γ	$\gamma+\delta$ (13.0)	$\gamma+\delta$ (10.0)	$\gamma+\delta$ (14.0)	$\gamma+\delta$ (20.0)	$\gamma+\delta$ (18.0)	$\gamma+\delta$ (97.0)	γ
	50.8	0.47	$\gamma+\delta$ (9.0)	$\gamma+\delta$ (2.0)	$\gamma+\delta$ (19.0)	γ	$\gamma+\delta$ (2.0)	$\gamma+\delta$ (95.0)	$\gamma+\delta$ 98.0	γ	$\gamma+\delta$ (3.0)	$\gamma+\delta$ (4.0)	$\gamma+\delta$ (21.0)	$\gamma+\delta$ (24.0)	$\gamma+\delta$ (10.0)	$\gamma+\delta$ (96.0)	γ
	127.0	1.2	γ	γ	$\gamma+\delta$ (18.0)	γ	γ	δ	δ	γ	γ	γ	$\gamma+\delta$ (10.0)	$\gamma+\delta$ (18.0)	γ	$\gamma+\delta$ (98.0)	γ
	190.5	1.8	γ	γ	$\gamma+\delta$ (8.0)	γ	γ	δ	δ	γ	γ	γ	$\gamma+\delta$ (3.0)	$\gamma+\delta$ (5.0)	γ	δ	γ
	254.0	2.3	γ	γ	$\gamma+\delta$ (3.5)	γ	γ	δ	δ	γ	γ	γ	$\gamma+\delta$ (1.0)	$\gamma+\delta$ (2.0)	γ	δ	γ

(a) [ ] Cr_{eq}/Ni_{eq} ratio.
(b) ( ) Volume % ferrite.

structures were examined by conventional light microscopy, paying special attention to the mode of solidification. Ferrite levels were evaluated optically by the point count method, taking three independent measurements for each condition, using a 10 × 10 grid. Electron microscopy was performed on thin foils with a JEOL 2000 FX electron microscope. The thin foils were taken from near the surface of the welds, in order to avoid any complications in specimens with only partial weld penetration. Phase identification was confirmed by electron diffraction.

Results and Discussion

Microstructure

The as-welded microstructures were categorized by optical microscopy into one of three groups: fully austenitic, duplex austenitic and ferritic, and fully ferritic. In addition, in those alloys where ferrite was present, the amount of ferrite was determined by using a point counting method. Significant changes in the microstructures, compared to conventionally welded materials, were found for various combinations of laser beam welding conditions. The results on all heats for both power levels and all welding speeds are summarized in Table 2. Rather than consider each alloy and condition separately, the results will be grouped according to trends that were identified.

Most of the alloys (Types 304, 308, 309, 312, 316, 347 and 446) consist of a duplex austenite plus ferrite microstructure following conventional welding. At the lowest laser beam welding speeds, these same duplex structures were observed. However, as the welding speed was increased, several different trends were noticed. For Types 304A, 304B, 308A, 308B, 316A, 347A and 347B, a decrease in the ferrite content was found as the welding speed increased. For these alloys, the decrease in ferrite content was gradual until a transition to a fully austenitic microstructure was noted. The welding speed at which the transition to a fully austenitic structure occurred varied according to the welding power level. For lower power levels, with correspondingly higher calculated cooling rates (Table 2), the transition typically took place at slower speeds. Furthermore, the transition often occurred at different welding speeds for different alloy heats. These effects are shown graphically in Fig. 2 for the 190- to 200-W power laser beam welds. The same trends were found for these alloys at the lower power level. A representative set of micrographs depicting this variation in ferrite content for Alloy 308 is given in Fig. 3. Electron microscopy revealed the presence of an occasional grain of ferrite in the structures characterized as fully austenitic by optical microscopy (Fig. 4). However, the overall ferrite content in the nominally fully austenitic structures was well below 1%.

For several of the alloys in this group, no clear evidence of a solidification substructure in the fully austenitic condition was evident — Fig. 3C. In contrast, for Type 316A alloy, a very well defined solidification microstructure was found by optical microscopy, as shown in Fig. 5A. Electron microscopy of the fully austenitic Types 308A and 316A welds indicated that the austenite grains were very fine. The dislocation densities for the two alloys were quite different, with a low density in the former alloy (Fig. 4) and a high density in the latter — Fig. 5B. These structures may suggest that possible recrystallization occurs during cooling subsequent to solidification and are the subject of further investigation.

A second group of alloys showed a different change in ferrite content with increasing cooling rate. For the Alloys 309A, 309B and 316B, a transition to a fully austenitic microstructure was not found. In addition, as the cooling rate increased, the ferrite content initially increased before eventually decreasing. This behavior is shown in Fig. 6 for the 110- to 120-W power laser welds. Again, the same trends were found for these alloys at the other power level. A typical series of micrographs revealing the variation in ferrite level with welding speed (cooling rate) is shown in Fig. 7 for laser

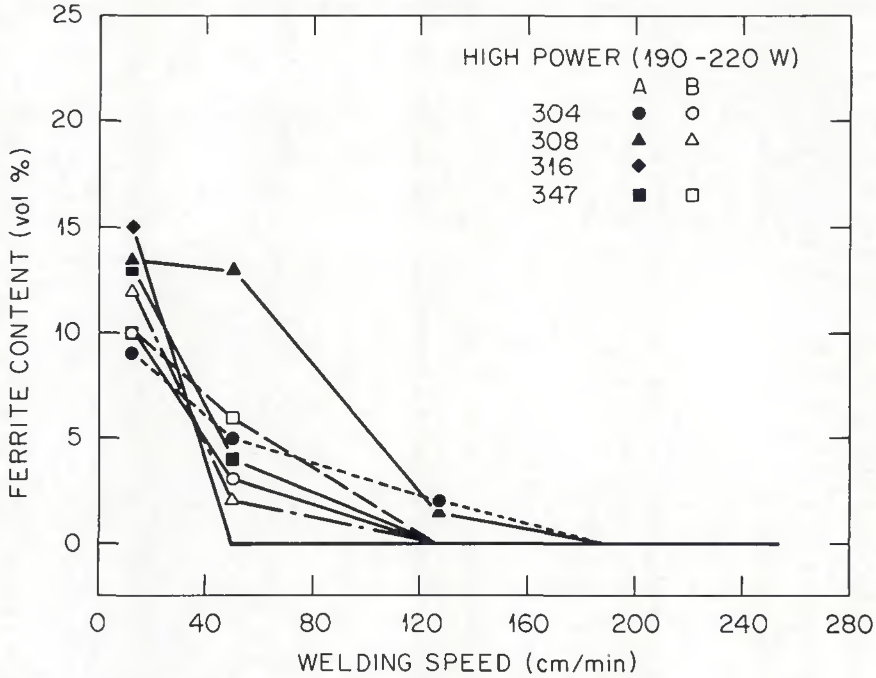

Fig. 2 — Decrease in ferrite content as a function of welding speed observed for several steels (190- to 200-W power level)

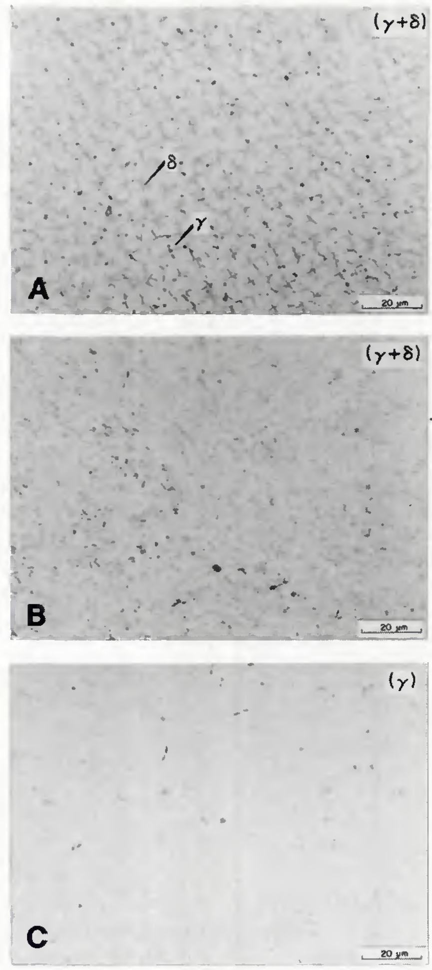

Fig. 3 — Microstructures of Type 308A laser beam welds (190- to 200-W power) showing the transition to a fully austenitic structure with increasing welding speed. A — 12.7 cm/min; B — 50.8 cm/min; C — 190.5 cm/min

Fig. 4 — TEM micrograph showing occasional ferrite and fine austenite grain size in the fusion zone of Type 30BB stainless steel laser beam welded at 127 cm/min (190- to 200-W power level)

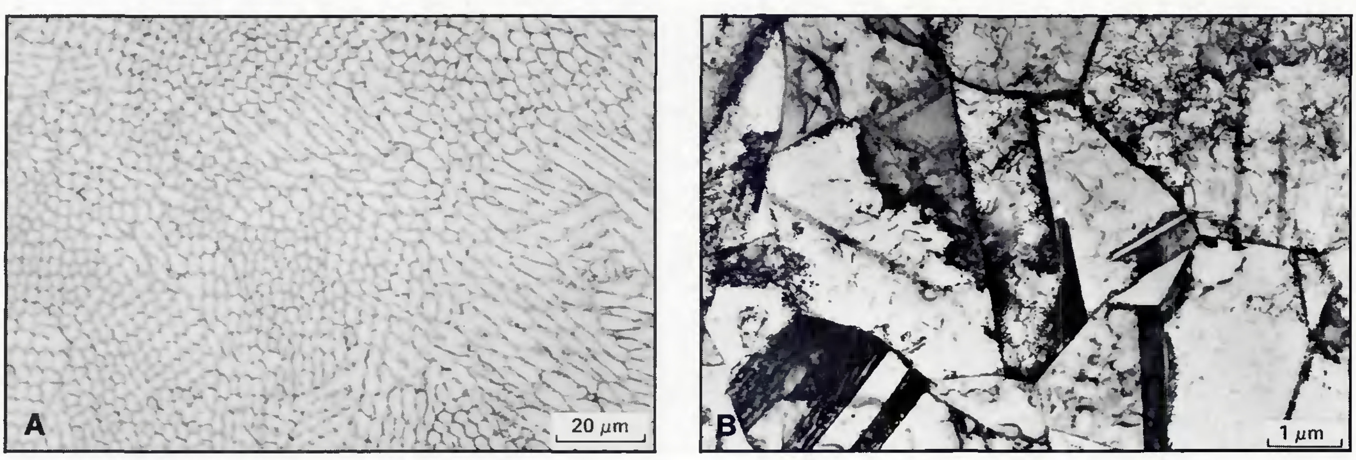

Fig. 5 — Fully austenitic microstructure of Type 316A stainless steel laser beam welded at 50.8 cm/min showing well-defined solidification structure and higher dislocation density. A — Optical; B — TEM micrographs

beam welded Type 309A. There was a noticeable change in the ferrite morphology at the higher welding speeds. Whereas the ferrite morphology was vermicular at the lower welding speeds, the ferrite was distributed more randomly and was more disconnected in the materials welded at a higher speed — Figs. 7A and 7B vs. Fig. 7C. Patchy areas of fully austenitic material were present, and these regions were found only at welding speeds beyond those corresponding to the maximum in the ferrite content vs. welding speed curve — Fig. 6.

Alloys 312A, 312B and 446 showed yet another dependence of structure on welding speed. In these alloys, as the welding speed increased, the ferrite content also increased, until a fully ferritic microstructure was obtained at the highest welding speeds. Under conventional welding conditions, 40 to 50% ferrite is typically present in the as-welded structure. However, under all of the laser beam welding conditions examined, significantly more ferrite was detected. A series of micrographs revealing this trend is shown in Fig. 8.

The fourth and final type of behavior with regard to ferrite variation with welding speed was found for Alloy 310. Under conventional welding conditions, this alloy is fully austenitic. For all of the laser beam welding conditions tested, no change in the structure was found. The structure was fully austenitic, as revealed in Fig. 9. The microstructure was predominantly cellular dendritic, with the size of the cells decreasing with increasing welding speed.

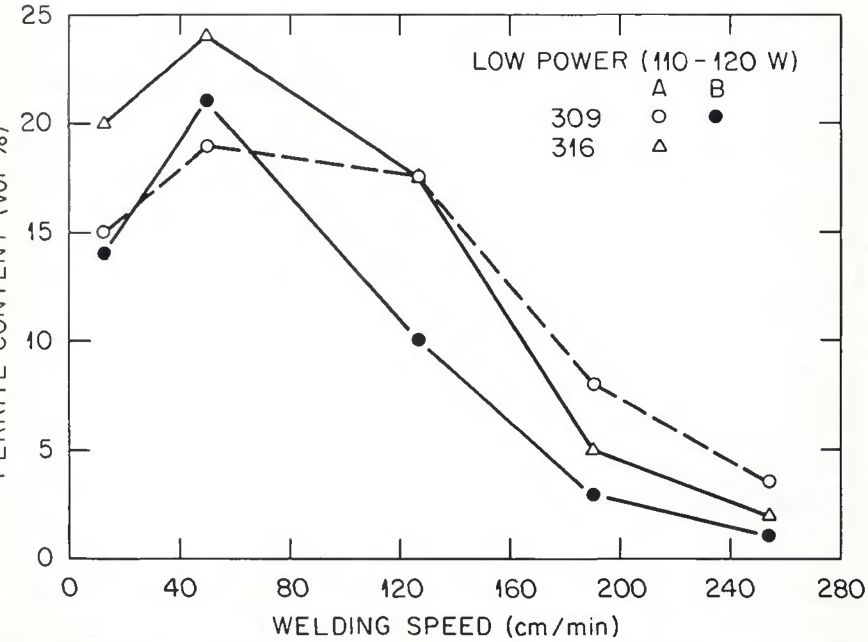

Fig. 6 — Initial increase and subsequent decrease in ferrite content as a function of welding speed found for several steels (110- to 120-W power level)

Significant variations in structure were often found among heats of the same alloy. This was particularly true for Types 309 and 316. In the case of Type 309, the same trend in ferrite content vs. welding speed behavior was found for both heats, but the amount of ferrite was noticeably greater for the 309B heat. This may be due to the presence of Ti, Ta or Nb in the 309B heat, all of which are ferrite stabilizers. The difference between Heats A and B of Type 316 steel was even more dramatic. The ferrite content vs. welding speed for these two heats is plotted in Fig. 10, and the microstructures are compared in Fig. 11. Whereas 316A showed a transition to a fully austenitic structure at higher welding speeds, no such transition was found for 316B. Thus, it is apparent that even if two heats remain within the compositional specifications of a given alloy, small changes in composition may lead to strik-

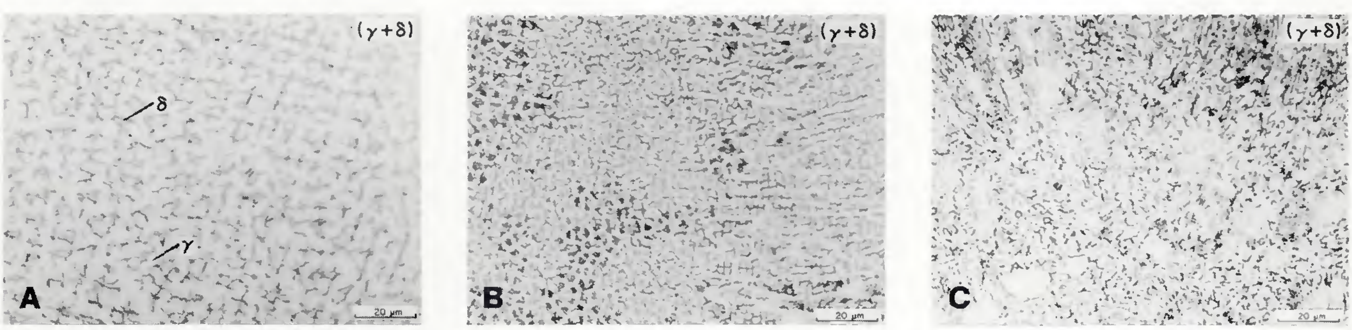

Fig. 7 — Microstructures of Type 309A laser beam welds (190 to 200 W) showing initial increase and eventual decrease in ferrite number with increasing welding speed. A — 12.7 cm/min; B — 50.8 cm/min; C — 190.5 cm/min

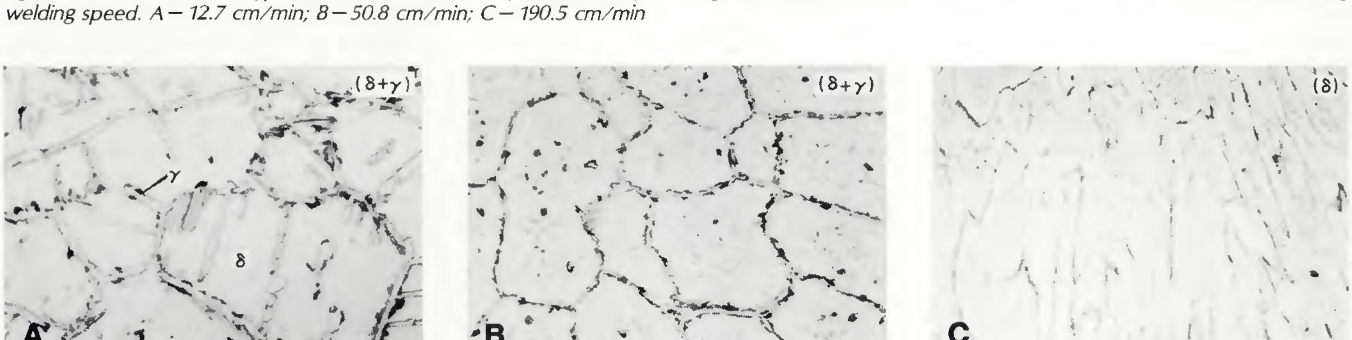

Fig. 8 — Micrographs revealing the transition to a fully ferritic structure in Type 312A laser beam welds as a function of welding speeds. A — 12.7 cm/min; B — 50.8 cm/min; C — 190.5 cm/min

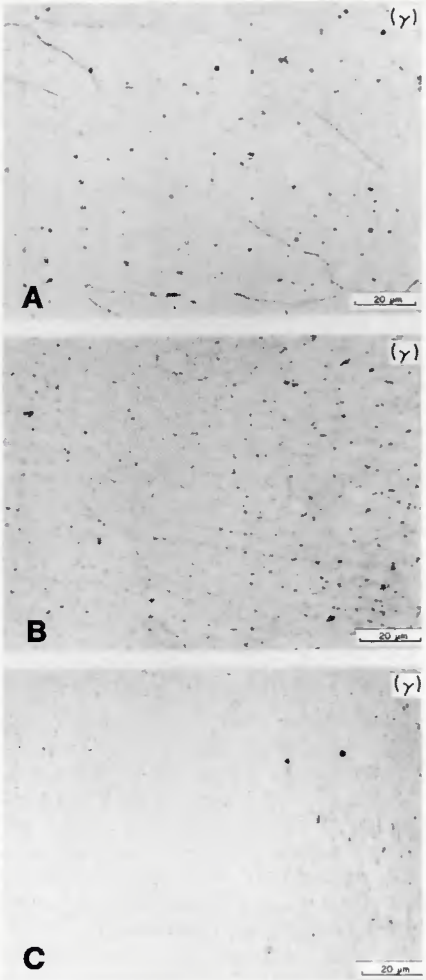

Fig. 9 — Fully austenitic microstructures of Type 310A laser beam welds found at all welding speeds. A — 12.7 cm/min; B — 50.8 cm/min; C — 190.5 cm/min

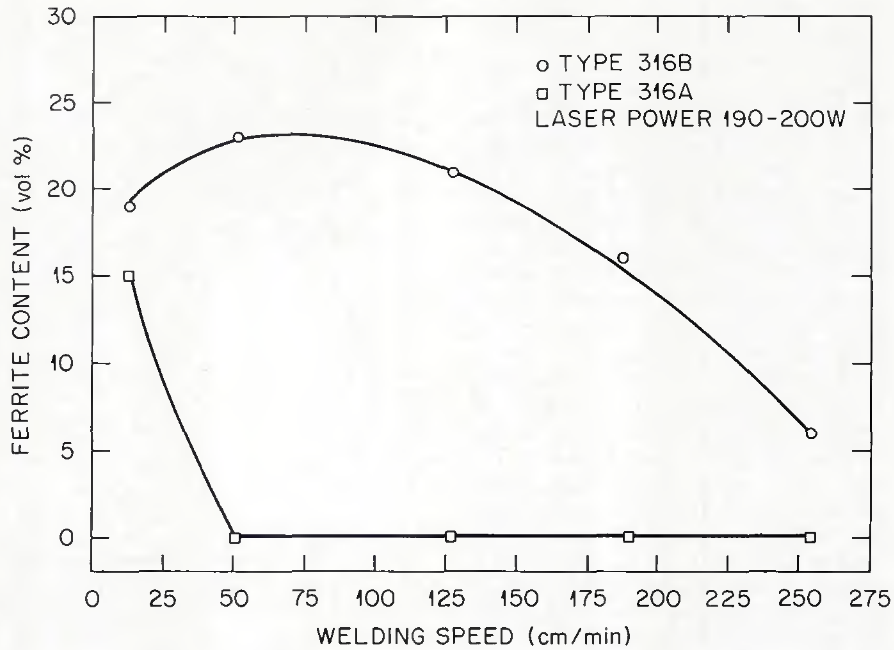

Fig. 10 — Heat-to-heat variation of the dependence of ferrite content on welding speed for Types 316A and 316B stainless steels

ing differences in the structures obtained after laser beam welding. The sensitivity to alloy composition will be discussed in more detail in the following sections.

Although a thorough analysis of hot cracking tendencies was not carried out, some important observations were made. Some cracks were found in the fully austenitic Type 310 alloy. In contrast, no cracking was found in any of the other alloys, *i.e.,* in the duplex austenite plus ferrite structures, the fully austenitic structures, or the fully ferritic structures. Therefore, it is clear that a fully austenitic structure does not necessarily have to be prone to hot cracking. These results confirm earlier work (Refs. 6, 7) in which cracking was also found in fully austenitic Type 310 laser beam welds, but not in fully austenitic Type 308 laser beam welds. The earlier work also showed some cracking tendencies in the fully ferritic Type 312 laser beam welds. Such cracking was not found in this investigation. A more detailed examination of hot cracking behavior in rapidly solidified stainless steels is presently under way in our laboratory, and the results will be reported at a later date.

Finally, small, Mn- and Si-rich, round inclusions were found in the laser beam welded structures. An example is shown in Fig. 12. Electron diffraction of these particles indicated they were amorphous in nature. Such amorphous MnSi particles had also been found in an earlier study (Refs. 6, 7). Recently, Eagar (Ref. 11) has shown that preferential evaporation may be a serious problem in welding. In fact, he indicated that manganese and silicon may be two species with a greater tendency toward evaporation during welding. Assuming this is the case for laser beam welding, it is hypothesized that the manganese and silicon vapors recondense on the wall of the keyhole formed during laser beam welding in the form of particles that are later incorporated into the structure. This mechanism explains the spherical shape of the particles.

Effect of Cooling Rate on the Mode of Solidification

An attempt was made to evaluate the cooling rates during solidification for the various laser beam welding conditions examined. Presently, no rigorous model based on first principles of transport phenomena is generally available. Consequently, simple calculations were made using the approach of Adams (Ref. 12) to provide a rough estimate of the cooling rates and to incorporate the effects of laser power and welding speed. Over the range of welding conditions investigated, penetration of the welds varied from full thickness to approximately one-quarter thickness. Therefore, the heat flow conditions varied from a 2D to 3D case, but the calculations were made using only the 3D case, which is appropriate for the higher cooling rate conditions. For the calculations, a laser absorptivity factor of 20% was used, based on the data in the literature (Ref. 13). Based on the pulse rate and duration, the duty cycle was 20%. Cooling rates were calculated for a liquidus temperature of 1450°C (2642°F) for all alloys. The results of the cooling rate calculations are given in Table 2. The cooling rates covered a range from 0.07 to 2.3×10^6 °C/s.

Although the absolute values of the calculated cooling rates may not be very accurate, the purpose of these calculations was to examine the trends between the cooling rate and the laser speed, power and microstructure. Such trends predicted by the Adams model should be reliable. Comparing the calculations to other estimates of cooling rates, the present calculations appear to be accurate to within an order of magnitude. The microstructures produced by laser beam welding for the higher cooling rates are similar to those found in splat quenched specimens (Ref. 7), for which the cooling rates have been estimated (Ref. 14) to be at least 10^6 °C/s. Others have estimated (Ref. 15) the cooling rates for laser beam welding to be on the order of 10^5 to 10^6 °C/s. This is in agreement with our approximate calculations. Finally, in one specimen, the secondary dendrite arms were discernible and the arm spacings could be approximated. The spacings can be related to cooling rates (Ref. 8). For a measured secondary dendrite arm spacing of 0.7 μm in a Type 310 stainless steel

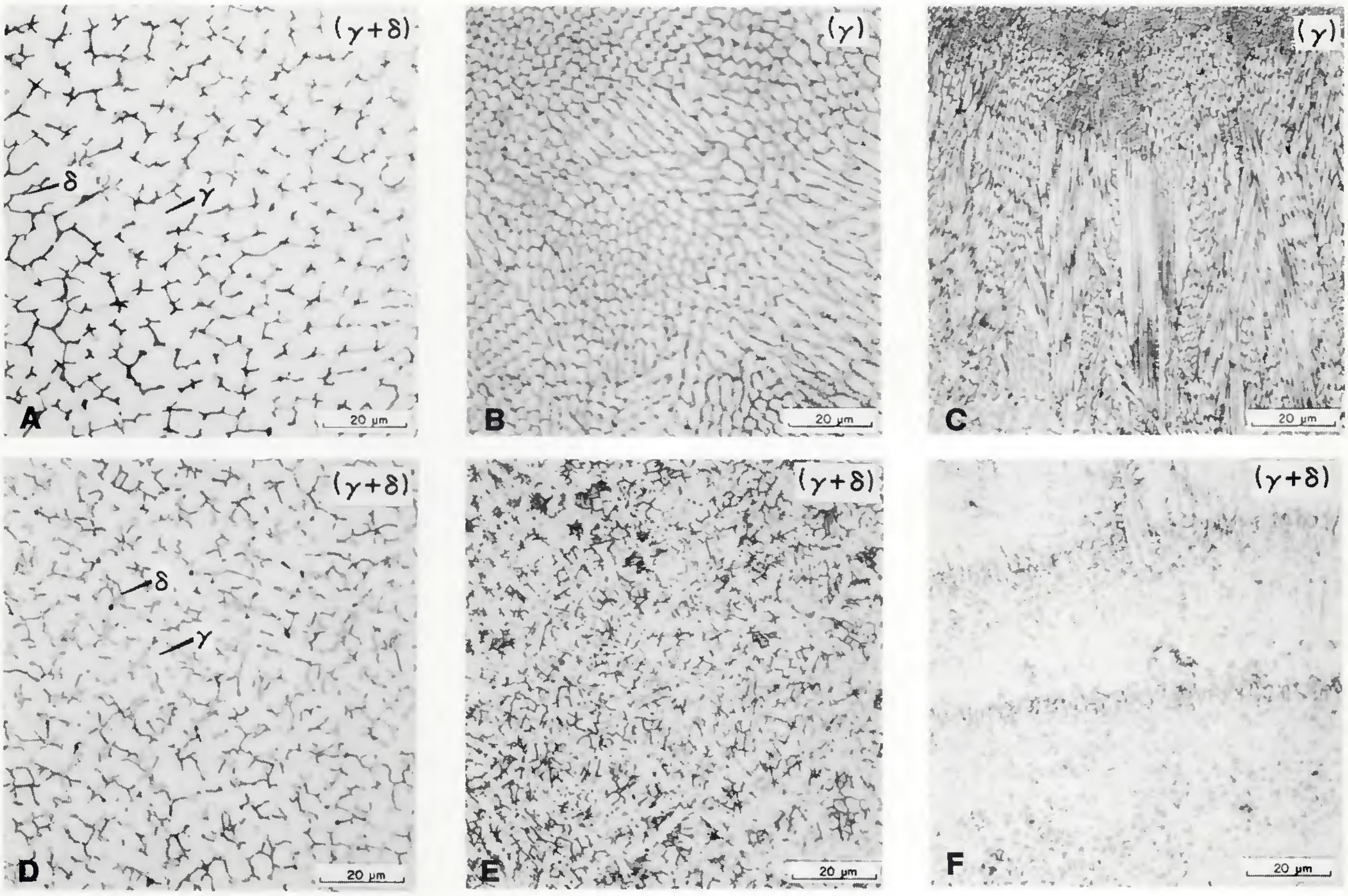

Fig. 11—Microstructures of Type 316A laser beam welds at: A — 12.7 cm/min; B—50.8 cm/min; C— 190.5 cm/min. Type 316B laser beam welds at: D— 12.7 cm/min; E—50.8 cm/min; F— 190.5 cm/min

specimen welded at 254 cm/min with a laser power of 200 W, a corresponding cooling rate of 7×10^5 °C/s was found to be in reasonable agreement with the calculated value of 1.4×10^6 °C/s.

Four types of solidification modes can be identified for the stainless steels under consideration (Ref. 16). These are ferritic (F), ferritic-austenitic (FA), austenitic-ferritic (AF), and austenitic (A). Briefly, these modes may be described as follows: F—primary ferrite solidification only; FA—primary ferrite solidification with austenite solidification at the later stages as a result of a peritectic reaction; AF—primary austenite solidification with some ferrite solidification as a result of solute segregation; A—primary austenite solidification only. A more complete description may be found in Ref. 13. The mode of solidification expected for each of the alloys under conventional welding conditions is given in Table 3. Most of the alloys evaluated solidify in either the F or FA modes during conventional welding processes. For these solidification modes, as the weld is cooled from elevated temperatures the ferrite becomes unstable and undergoes a solid-state transformation to austenite (Ref. 17). Since the cooling rates even under conventional welding conditions are relatively high

Fig. 12—TEM micrograph showing ferrite and amorphous Mn-Si particles in Type 316A, laser beam welded at 12.7 cm/min

Table 3—Modes of Solidification

Alloy	Solidification Mode[a]	Cr_{eq}/Ni_{eq}
304A	FA	1.67
304B	FA	1.74
308A	FA	1.76
308B	FA	1.52
309A	FA	1.61
309B	FA	1.58
316A	FA (AF)[b]	1.45
316B	FA (AF)[b]	1.51
312A	F	2.29
312B	F	2.36
347A	FA	1.66
347B	FA	1.91
446	F	5.36
310A	A	1.09
310B	A	1.29

(a) A = single phase austenitic; AF = austenitic-ferritic; FA = ferritic-austenitic; F = single-phase ferritic.
(b) Generally shows a mixed mode of freezing, FA-AF.

($>10^2$ °C/s), the solid-state transformation of ferrite to austenite is normally not completed, and some residual ferrite remains in the as-welded structure. If the cooling rates are increased substantially, as in the case of laser beam welding, then one might expect this solid-state transformation to be retarded, or even suppressed completely. This is precisely what happens for the Types 312 and 446 alloys. The amount of residual ferrite present in the as-welded condition is significantly greater for laser beam welds than the typical ferrite content of 40 to 50% found in conventionally welded materials. Furthermore, with higher cooling rates, the ferrite to austenite solid-state reaction is suppressed completely, yielding a fully ferritic microstructure.

The increase in the ferrite content with increasing cooling rate is also found at the lower welding speeds for Alloys 309A, 309B and 316B. However, as the welding speed is increased even further, this trend is reversed (see Fig. 6). This decrease in ferrite content with increasing cooling rates, observed at the higher cooling rates, cannot be explained by assuming the solid-state transformation is simply retarded at the higher cooling rates. A decrease in the ferrite content with increasing cooling rate is observed for several other alloys (Types 304, 308, 347 and 316 Heat A) at all welding speeds. In this latter group, the ferrite level eventually decreases to zero beyond some critical cooling rate, the value of which is both alloy and heat dependent. The fully austenitic weld metal structures observed in this latter group of steels must be due to a change in the mode of solidification to one of primary austenite formation (A mode). For intermediate cooling rates which are insufficient to produce a fully austenitic structure, one of two possibilities may occur.

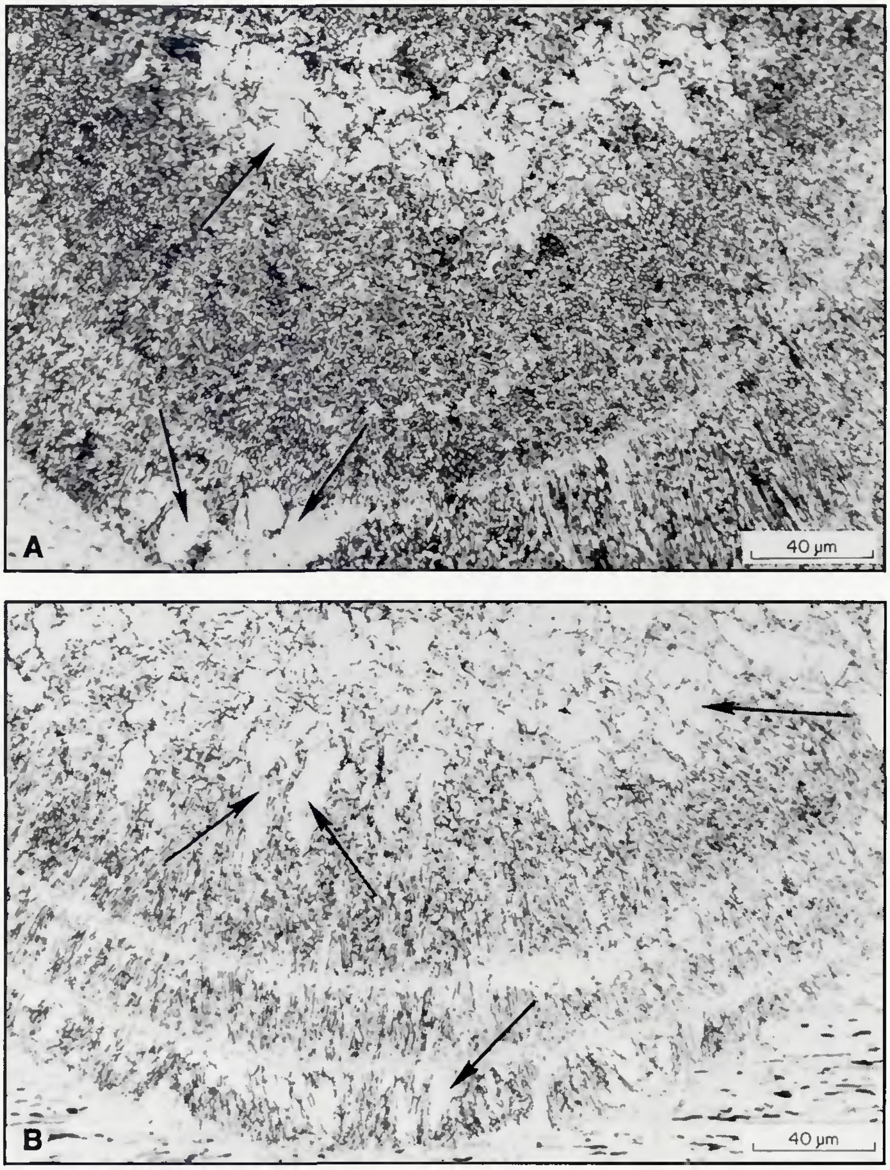

Fig. 13—Microstructures of Type 309B laser beam welds showing fully austenitic regions that increase in volume percent with increasing welding speed. A — 127 cm/min; B — 190.5 cm/min

Due to segregation during solidification, some ferrite may form in the intercellular regions, resulting in an AF mode of solidification. Some evidence of such a sequence can be seen in Figs. 3C and 4, where very small quantities of intercellular ferrite can be identified. Alternatively, a mixed mode of solidification may occur, with a combination of either AF + FA, or A + FA. Such a structure would consist of patches corresponding to the different solidification modes. The disconnected ferrite morphology shown in Fig. 7C may be caused by such a mixed mode of solidification. More striking evidence for a mixed mode of solidification is shown in Fig. 13, where very distinct patches of fully austenitic regions are clearly visible within a duplex austenite plus ferrite matrix. Mixed mode solidification in Type 316 steel has also been identified previously (Ref. 18). These alternative solidification mechanisms can readily explain the gradual decrease in ferrite content with increasing cooling rate found for cooling rates below the critical cooling rate necessary to produce a fully austenitic structure.

The behavior of Types 309A, 309B and 316B steels is atypical in that a fully austenitic structure is not found over the entire range of cooling rates evaluated. This is simply an indication that the critical cooling rate necessary to solidify these alloys entirely in the primary austenite mode was not achieved under the conditions tested. The results support this idea. First, the fact that the ferrite content decreases with increasing cooling rate at the higher cooling rates demonstrates that the critical cooling rate is being approached. Second, Fig. 13 clearly shows fully austenitic regions, again indicating that the cooling rate is very close to the critical rate needed for a fully austenitic structure. Furthermore, Fig. 13 shows that the volume percent of fully austenitic regions increases with increasing welding speed. It is noteworthy that a fully austenitic structure was produced in Alloy 316A at relatively low cooling rates, indicating a very sensitive dependence of the critical cooling rate on composition.

The competition between primary austenite formation and primary ferrite formation, and the effect that solidification rate may have, can be readily understood by referring to a schematic vertical section of the Fe-Cr-Ni phase diagram. Such a section is shown in Fig. 14, with lines approximately representing three austenitic steel compositions superimposed. The T_o lines (Ref. 19) representing partitionless solidification of either austenite or ferrite have also been sketched. The T_o lines represent the loci of temperatures below which the single phase austenite (or ferrite) has a lower free energy than the single phase undercooled liquid. The T_o lines must lie within the $(L + \gamma)$ or the $(L + \delta)$ phase fields and they have been schematically extended to cover a wider range of alloy compositions.

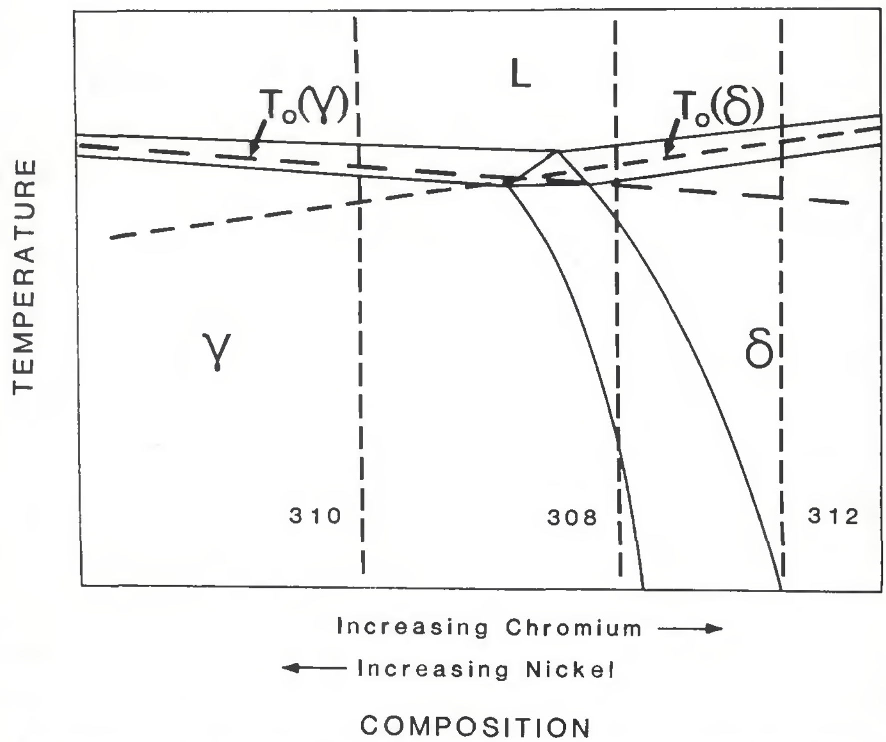

Fig. 14 — Schematic diagram of a vertical section of the Fe-Cr-Ni phase diagram, with schematic T_o lines for partitionless ferrite or austenite solidification superimposed. Approximate compositions of three alloys are qualitatively indicated for discussion purposes

For alloys that normally solidify in the F mode, such as the Type 312 steel, undercooling during laser beam welding may be sufficient to bring the liquid below the ferrite T_o line. Thus, the only solidification mode available upon cooling is the F mode. On the other side of the diagram, alloys that normally solidify in the A mode, such as Type 310, continue to solidify in this mode because the undercooling during rapid solidification is likely to be great enough to bring the liquid below the austenite T_o line, but not below the ferrite T_o line. Therefore, only partitionless austenite formation is possible. For intermediate compositions, such as those for Types 308, 304, 309, 347 and 316 steels, the undercooling achieved during rapid solidification may be sufficient to bring the liquid below the T_o lines of both austenite and ferrite (Ref. 20). If this occurs, the actual mode of solidification will depend on the relative kinetics of nucleation for austenite and ferrite. Kelly, *et al.* (Ref. 9), have addressed the issue of the relative nucleation rates for austenite and ferrite. They have found that in the presence of heterogeneous nucleation sites, which are readily available in larger solidification volumes such as those in the present study, austenitic solidification is kinetically favored. Although their analysis was for Type 303 stainless steel, it is possible that the same conclusions may be applicable to austenitic stainless steels in general. Therefore, if a critical undercooling is achieved such that the liquid is brought below the T_o lines for both austenite and ferrite, the austenite solidification will be dominant because of the faster kinetics for this reaction. Thus, for the Alloys 304, 308, 347 and 316A, the laser beam welding conditions were presumably sufficient to undercool the liquid below the austenite T_o line, resulting in a change in the solidification mode to that of primary austenite formation. Apparently, such a critical undercooling was not achieved in the case of the 309 and 316B steels.

The interpretation of the results has been based on the assumption that, when possible, partitionless solidification will occur. However, some solute partitioning has been observed by analytical electron microscopy, and can be inferred from the presence of intercellular ferritic areas such as those in Figs. 3 and 4. The degree of partitioning is expected to be a function of the laser beam welding speed. However, the presence of a small amount of partitioning should not influence, in any major way, the conclusions that were drawn. The concept of partitionless solidification is still a simple and useful way of understanding the observed behavior, and the small degree of partitioning present in the rapidly cooled laser beam welds can be considered as a small perturbation on these conclusions.

A change in the mode of solidification with cooling rate has been observed to a limited extent before. Earlier work on three stainless steels showed that laser beam welding, as well as splat quenching, can change the mode of solidification from that of primary ferrite to one of primary austenite formation (Ref. 7). It was found that a change in solidification mode was very sensitive to cooling rate for rates on the order of 10^6 °C/s, comparable to the cooling rates calculated for the laser beam welding conditions in this study. Within a splat quenched foil in which no detectable change in composition through the thickness was measured, a change in the mode of solidification was found between the surface of the foil and the slightly slower cooled foil interior. In addition, a change in solidification mode was found between the root and crown of a single autogenous laser beam weld. Such a sensitivity to cooling rate agrees with the findings in the present study. Suutala (Ref. 21) also found some evidence for a change in the mode of solidification in gas tungsten arc (GTA) welds. He observed that at higher solidification rates the mode changed from one of primary ferrite to that of a mixed primary ferrite and primary austenite. Presumably, the cooling rates prevalent during GTA welding were insufficient to obtain a fully austenitic structure. Suutala concluded that under the welding conditions he employed, cooling rates played only a minor, secondary role to that of composition in determining the mode of solidification. Lippold (Ref. 22), on the other hand, found a change in the solidification mode from primary ferrite to primary austenite that resulted in a fully austenitic structure at the weld centerline of elec-

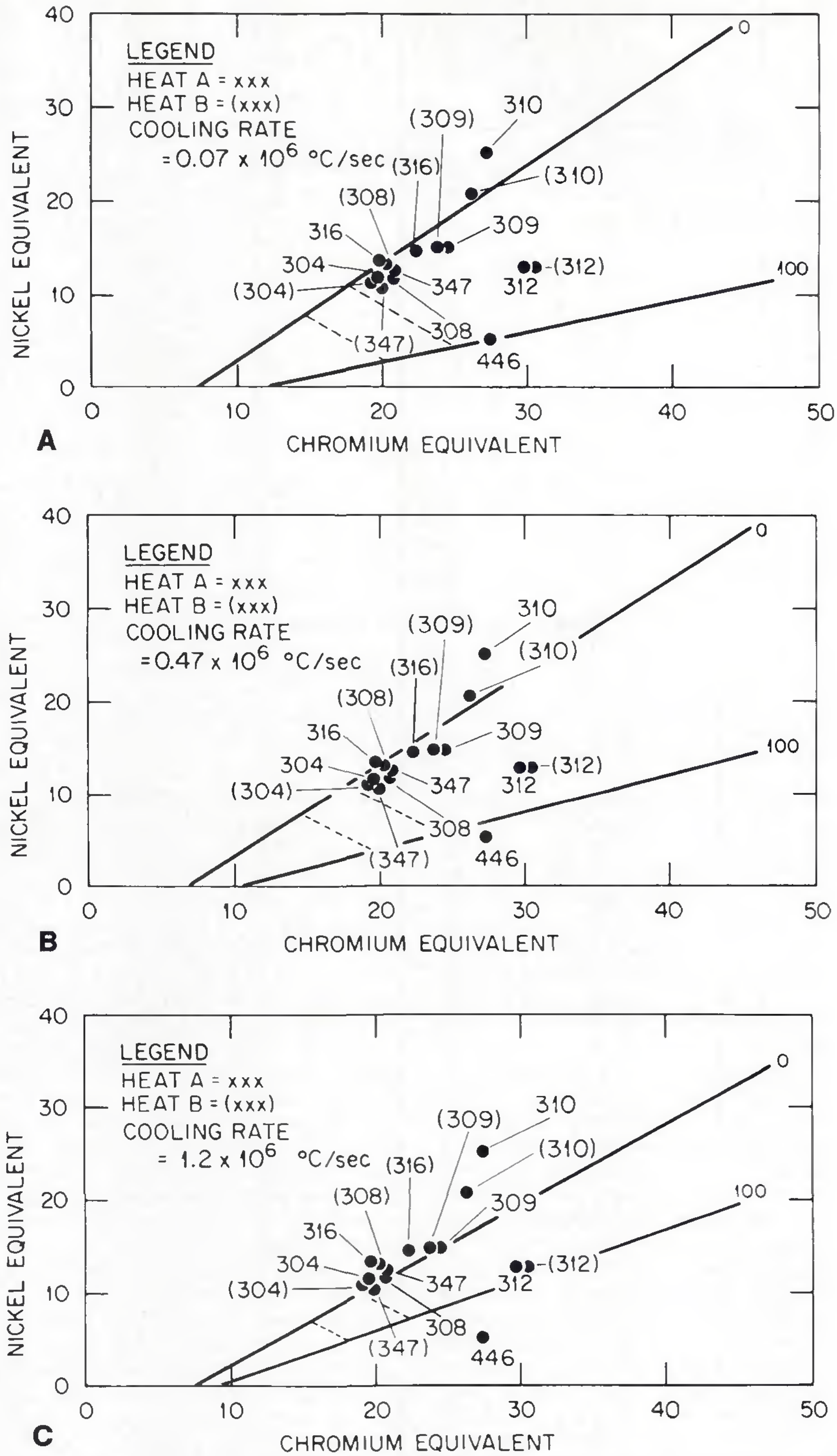

Fig. 15 – Cooling rate modified Schaeffler diagrams showing the convergence of the 0 and 100% ferrite lines as the cooling rate increases

tron beam welds of Type 304L stainless steel. He associated the presence of a fully austenitic structure with the areas subjected to the highest solidification rates, in agreement with the findings in the present and earlier studies (Refs. 6, 7).

Implications on the Schaeffler Diagram

Since it is clear from the observations that cooling rate plays a major role in determining the solidification mode and the final microstructure of rapidly solidified welds, an attempt has been made to incorporate the results of this study into the Schaeffler diagram by adding cooling rate as a new dimension. In the Schaeffler diagram, each of the limited number of constant ferrite content contour lines may be described by the following relation:

$$(Ni_{eq} - Ni_o) = S\,(Cr_{eq} - Cr_o) \qquad (1)$$

where Ni_{eq} and Cr_{eq} are the nickel and chromium equivalents defined for the Schaeffler diagram (S is the slope of the contour line, and Ni_o and Cr_o are the nickel and chromium equivalent composition coordinates of the intersection of the 0% and 100% ferrite contour lines).

The effect of cooling rate was introduced by considering only the 0 and 100% ferrite contours and allowing these contours to change with increasing cooling rate. The intersection of these two contours was kept constant at the same point as in the original Schaeffler diagram, and the contours were also assumed to remain straight lines. As the cooling rate increases, the 0 and 100% contours were allowed to change to the positions of the contour lines corresponding to F and F′ percent ferrite, respectively, in the original Schaeffler diagram. The procedure for incorporating the effect of cooling rate is quite simple; available data do not warrant the use of a more complicated model. The expressions for the 0 and 100% ferrite contours in terms of F and F′ are:

$$F = 8.5\, R_c \qquad (2)$$

and

$$F' = 100 - 25\, R_c \qquad (3)$$

respectively, where F and F′ represent the corresponding contour lines for the percent ferrite in the original Schaeffler diagram and R_c is the cooling rate (°C/s) $\times 10^{-6}$ ($0.01 < R_c < 2.3$). These equations represent a fit for all of the 15 alloy compositions and 10 cooling rates investigated. It should be remembered that these equations are limited by the accuracy of the estimated cooling rates.

The modified Schaeffler diagrams at higher cooling rates are presented in Fig. 15. At the lowest cooling rate considered (0.07×10^6 °C/s) (Fig. 15A), there is very little change in the location of the contour lines compared to the positions in the original diagram – Fig. 1. This is a reflection of the fact that at the lower cooling rates evaluated in this study, the structures were comparable to those found under conventional welding conditions. This also agrees with the conclusion of others (Ref. 21) that at low cooling rates the structure is very weakly dependent on cooling rate. However, as the cooling rate increases, it is evident that the two contour lines must converge in order to fit with the experimental results. This is shown in Figs. 15B and 15C. Composi-

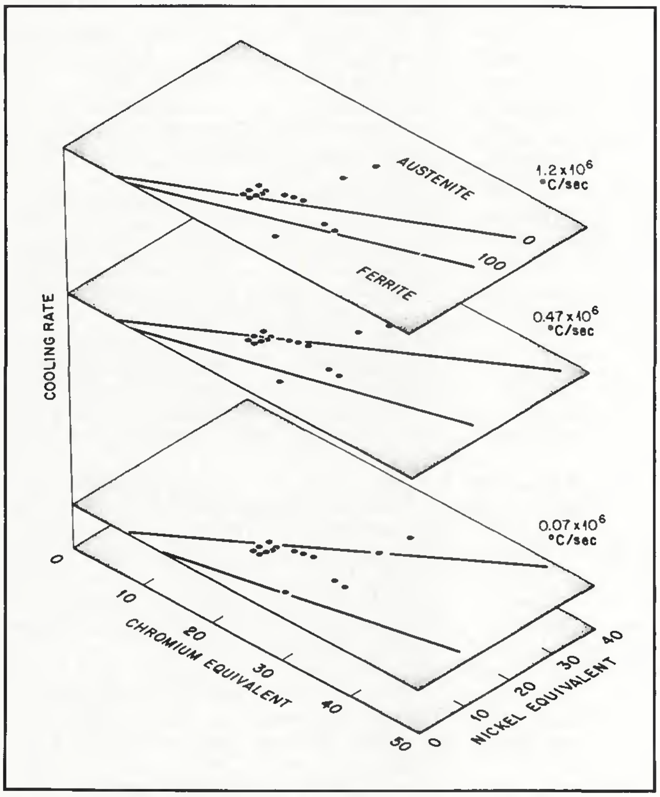

Fig. 16 — Proposed composite constitution diagram for welds using cooling rate as a third dimension

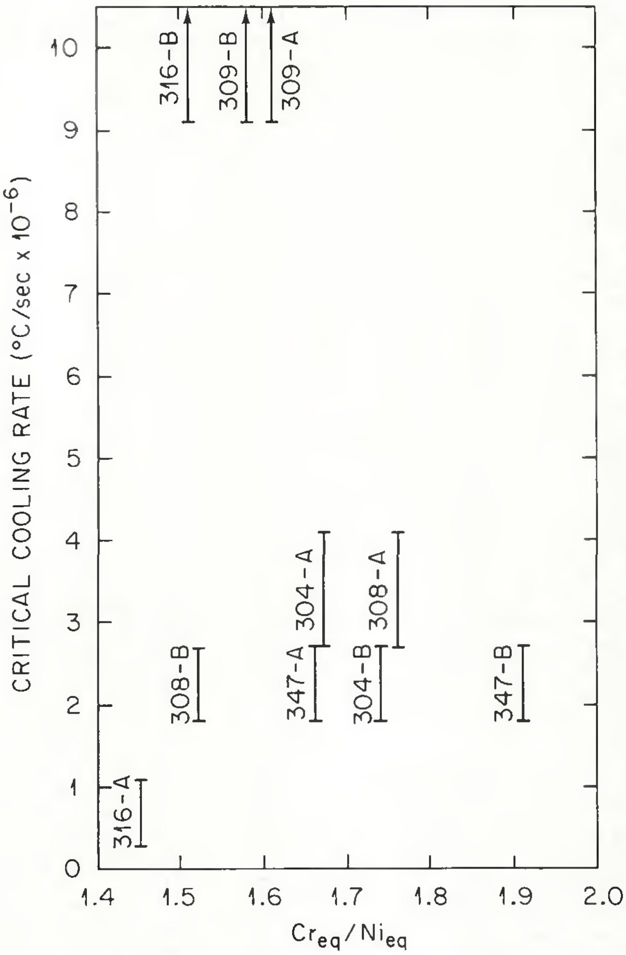

Fig. 17 — Estimated range of critical cooling rates for the transition to fully austenitic microstructures as a function of Cr_{eq}/Ni_{eq} ratio for several austenitic stainless steels

tions that were within the two-phase field in the original diagram now may lie outside the two contour lines, indicating that the structures are no longer duplex austenite plus ferrite, but rather single-phase austenite or single-phase ferrite. A composite diagram showing cooling rate as a third dimension for the constitution diagram for welds is shown in Fig. 16.

Some discrepancies do exist. For example, at the highest cooling rate (Fig. 15C), it was not possible to include Alloys 309A, 309B and 316B into the two-phase region, where they belong, without either deviating from straight contours, or by including several single-phase austenite compositions into the two-phase area, or moving the intersection of the 0 and 100% ferrite lines. Thus, it is apparent that a simple representation like the Schaeffler diagram does not work at all cooling rates. This may be an indication of one of several things. First, it is entirely possible that straight contour lines are an oversimplification, and more complicated curves must be invoked. Alternatively, the restriction that the intersection of the 0 and 100% ferrite lines remains the same may be incorrect. It is also possible that the relations defining the nickel and chromium equivalents are inaccurate, at least at the higher cooling rates. It is quite possible that other, minor alloying additions must be incorporated into the nickel and chromium equivalent expressions, or that the coefficients are not optimal. This latter alternative is a very real possibility since several other expressions for the appropriate coefficients have been proposed (Ref. 23). At the present time, we cannot ascertain which of these factors are dominant.

The possibility that the coefficients for the nickel and chromium equivalents need modification is supported by examining the dependence of the critical cooling rate for the transition to a fully austenitic structure on the Cr_{eq}/Ni_{eq} ratio. Given the calculated cooling rates in Table 2, one can arrive at upper and lower bounds for the critical cooling rates necessary to yield a fully austenitic structure. These ranges for the critical cooling rates have been plotted as a function of the Cr_{eq}/Ni_{eq} ratio in Fig. 17. For equivalent ratios of 1.4 to 1.8, a reasonable monotonic dependence of critical cooling rate on equivalent ratio for Alloys 304A, 304B, 308A, 308B, 316A and 347A is found. However, this relation breaks down for 347B, at higher chromium to nickel equivalent ratios, as well as for Alloys 309A, 309B and 316B. It seems apparent that modifications to the formulas for calculating the nickel and chromium equivalents must be made in order to achieve any kind of reasonable relationship between composition and critical cooling rate.

Conclusions

A wide variety of austenitic stainless steel laser beam welds were made at various welding speeds to cover a range of weld metal cooling rates. The microstructures were evaluated, and the results and conclusions are summarized as follows:

1. Rapid solidification of austenitic stainless steel weld metals shows extensive modifications in their microstructures. The microstructures ranged from duplex $\gamma + \delta$ to fully austenitic and fully ferritic. The microstructures were cooling

rate and composition sensitive.

2. Fully austenitic microstructures were produced in Types 304, 308, 347 and 316 (Heat A) laser beam welds that are otherwise duplex $\gamma + \delta$ after conventional welding. All of these steels showed a decrease in ferrite level with increase in laser beam welding speed or corresponding cooling rates.

3. Fully ferritic microstructures were produced in steels with high Cr_{eq}/Ni_{eq} ratios, such as Types 312 and 446 steel, that are also otherwise duplex $\gamma + \delta$ after conventional welding.

4. Substantial variations in microstructures were found from heat to heat. While it was possible to produce a fully austenitic microstructure in one heat of Type 316 steel (A) beyond a critical cooling rate, another heat (B) remained duplex $\gamma + \delta$ at all cooling rates.

5. Types 309A, 309B and 316B were always found to be duplex under the conditions investigated. In these steels, the ferrite content initially increased with increasing cooling rate and then decreased to a large extent. However, no fully austenitic microstructures were observed.

6. The observed microstructural modifications are mainly due to changes in the primary mode of solidification at large undercoolings and/or subsequent suppression of solid-state transformations. The normally duplex steels that readily produce fully austenitic microstructures undergo a change in the mode of solidification from primary ferrite to primary austenite at high cooling rates and associated large undercoolings. The steels that are fully ferritic do not change the mode of solidification from primary ferrite. However, because of the rapid cooling rates, the postsolidification ferrite to austenite solid-state transformation is suppressed, resulting in a fully ferritic microstructure. In some steels, evidence for a mixed austenite-ferrite mode of solidification was also observed.

7. Cooling rate effects were incorporated into modifications of the Schaeffler diagram to reflect the observed changes at high cooling rates of the weld metal. The Cr_{eq} and Ni_{eq} as used in the Schaeffler diagram do not seem to fully describe the ferrite-forming tendency as a function of cooling rate.

Acknowledgments

The authors would like to thank R. W. Reed for preparing the specimens and welding. They also thank J. F. King and J. A. Horton for reviewing the manuscript and Prof. T. DebRoy of Pennsylvania State University for assisting in the cooling rate calculations. Thanks are due to Kathy Gardner for preparing the manuscript. This research was sponsored by the Division of Materials Sciences, United States Department of Energy, under contract DE-AC05-84OR21400 with Martin Marietta Energy Systems, Inc.

References

1. Schaeffler, A. L. 1949. Constitution diagram for stainless steel weld metal. *Metal Progress* 56(5):680-680B.

2. DeLong, W. T. 1974. Ferrite in austenitic stainless steel weld metal. *Welding Journal* 53(7):273-s to 286-s.

3. Hull, F. C. 1973. Delta ferrite and martensite formation in stainless steels. *Welding Journal* 52(5):193-s to 203-s.

4. Pryce, L., and Andrews, K. W. 1960. Practical estimation of composition balance and ferrite content in stainless steels. *J. Iron Steel Inst.* 195:415.

5. Schoeffer, E. A. 1977. Constitution diagram for stainless steel castings. *Metal Progress Data Book* 51.

6. David, S. A., and Vitek, J. M. 1982. Solidification behavior and microstructural analysis of austenitic stainless steel laser welds. *Lasers in Metallurgy*, eds. K. Mukherjee and J. Mazumder, TMS-AIME, Warrendale, PA, pp. 247-254.

7. Vitek, J. M., Das Gupta, A., and David, S. A. 1983. Microstructural modification of austenitic stainless steels by rapid solidification. *Metall. Trans.* 14A:1833-1841.

8. Katayama, S., and Matsunawa, A. 1983. Solidification microstructures of laser welded stainless steels. *Proc. of ICALEO 84*, Vol. 44, L.1.A., pp. 60-67.

9. Kelly, T. F., Cohen, M., and Vander-Sande, J. B. 1984. Rapid solidification of a droplet-processed stainless steel. *Metall. Trans.* 15A:819-823.

10. MacIssac, M., Shiohara, Y., Chu, M. G., and Flemings, M. C. 1983. Structure of undercooled iron and nickel based alloys. *Grain Refinement in Castings and Welds*, eds. G. J. Abbaschian and S. A. David, TMS-AIME, Warrendale, PA, pp. 87-95.

11. Eagar, T. W. 1982. Massachusetts Institute of Technology, Cambridge, Mass. Private communication.

12. Adams, Jr., C. M. 1958. Cooling rates and peak temperatures in fusion welding. *Welding Journal* 37(5):210-s to 215-s.

13. Khan, P. A. A., and DebRoy, T. 1985. Absorption of CO_2 laser beam by AISI 4340 steel. *Metall. Trans. B*, Vol. 168, pp. 853-856.

14. Kroeger, D. M., Coghlan, W. A., Easton, D. S., Koch, C. C., and Scarbrough, J. O. 1982. A study of cooling rates during metallic glass formation in a hammer and anvil apparatus. *J. Appl. Phys.*, Vol. 53, pp. 1445-1453.

15. Weinman, L. S., and DeVault, J. N. 1979. A microprobe study of rapidly solidified laser surface alloyed low carbon steels. *Laser-Solid Interactions and Laser Processing—1978*, eds. S. D. Ferris, H. J. Leamy and J. M. Poate, Amer. Inst. of Physics, New York, N.Y., pp. 239-242.

16. Suutala, N. 1982. Solidification studies on austenitic stainless steels. *Acta Universitatis Ouluensis*, Series C, Technica No. 23, Metallurgica No. 3, University of Oulu, Finland.

17. David, S. A., Braski, D. N., and Goodwin, G. M. 1979. Solidification behavior of austenitic stainless steel filler metals. *Welding Journal* 58(11):330-s to 336-s.

18. Kujanpää, V. P., David, S. A., and White, C. L. 1986. Formation of hot cracks in austenitic stainless steel welds—solidification cracking. *Welding Journal* 65(8):203-s to 212-s.

19. Mehrabian, R. 1982. Rapid solidification. *Int. Metals Review* 27:185-208.

20. Jena, A. K., Giessen, B. C., Bever, M. B., and Grant, N. J. 1968. The metastability of gold-antimony phases prepared by splat cooling. *Acta Met.* 16:1047-1051.

21. Suutala, N. February 1983. Effect of solidification conditions on the solidification mode in austenitic stainless steels. *Met. Trans.* 14A:191-197.

22. Lippold, J. C. May 1985. Centerline cracking in deep penetration electron beam welds in type 304L stainless steel. *Welding Journal* 64(5):127-s to 136-s.

23. Suutala, N. 1982. Effect of manganese and nitrogen on the solidification mode in austenitic stainless steel welds. *Metall. Trans.* 13A:2121-2130.